3898 *Chem. Mater.* **2009,** *21,* 3898–3904
DOI:10.1021/cm901495h

CHEMISTRY OF MATERIALS
Article

Sb-MO_x-C (M = Al, Ti, or Mo) Nanocomposite Anodes for Lithium-Ion Batteries

Sukeun Yoon and Arumugam Manthiram*

Electrochemical Energy Laboratory & Materials Science and Engineering Program, University of Texas at Austin, Austin, Texas 78712

Received May 31, 2009. Revised Manuscript Received July 13, 2009

Sb-MO_x-C (M = Al, Ti, and Mo) nanocomposites have been synthesized by a mechanochemical reduction of Sb_2O_3 with, respectively, Al, Ti, and Mo, in the presence of carbon (acetylene black). X-ray diffraction (XRD), X-ray photoelectron spectroscopy (XPS), transmission electron microscopy (TEM), and scanning transmission electron microscopy (STEM) data reveal that these nanocomposites are composed of uniformly dispersed nanostructured antimony in the amorphous Al_2O_3, TiO_2, or MoO_3 matrix, along with conductive carbon. These composite electrodes exhibit excellent electrochemical cycling performance and rate capability in lithium cells, compared to pure antimony. Among the three Sb-MO_x-C systems studied, the M = Al system with Al_2O_3 as the amorphous phase exhibits the best electrochemical performance, offering a capacity of > 430 mAh/g after 100 cycles. The improvement in the cycling performance, compared to that of pure antimony, is attributed to a homogeneous distribution of the electrochemically active Sb nanoparticles within the ceramic oxide and conductive carbon matrix, resulting in good electrical contact with the current collector, as well as a mechanical buffering effect on the volume expansion−contraction that occurs during cycling.

Introduction

Lithium-ion batteries are being widely used as power sources for portable electronic devices such as cell phones, laptops, and personal digital assistants (PDAs). They are also pursued intensively for plug-in hybrid electric vehicle applications. However, the currently used layered $LiCoO_2$ cathode and the carbon anode have the drawbacks of limited energy density and safety concerns. Particularly, chemical instability arising from an overlap of the Co:3d band with the top of the O:2p band in the $LiCoO_2$ cathode, the formation of solid−electrolyte interfacial (SEI) layer by a reaction of the carbon anode surface with the electrolyte, and lithium plating in carbon anode arising from a charge/discharge potential close to that of Li/Li^+ pose serious safety concerns. These difficulties have created enormous interest in the development of alternate cathode and anode materials for lithium-ion batteries.[1−3]

With respect to alternative anodes, antimony alloys are appealing, because they offer high theoretical capacity (gravimetric and volumetric) and an operating voltage well above that of metallic lithium. Unfortunately, the reaction of antimony with lithium to form Li_3Sb is accompanied by a large volume change of 137%,[4−8] which results in cracking and crumbling of the alloy particles, disconnection of the electrical contact between the particles and current collectors, and consequent capacity fade during cycling.[9,10] To alleviate this problem, antimony-containing intermetallic compounds such as Cu_2Sb,[11] CoSb,[12] CrSb,[13] and MnSb[14] (in which only Sb is electrochemically active), SnSb,[15−17] InSb,[18] Zn_4Sb_3,[19] and AlSb,[20] in which both the metals are electrochemically

*Author to whom correspondence should be addressed. Phone: (512) 471-1791. Fax: (512) 471-7681. E-mail: rmanth@mail.utexas.edu.

(1) Megahed, S.; Scrosati, B. *J. Power Sources* **1994**, *51*, 79.
(2) Aricò, A. S.; Bruce, P. B.; Scrosati, B; Tarascon, J.-M.; Schalkwijk, W. V. *Nat. Mater.* **2005**, *4*, 366.
(3) Bruce, P. G.; Scrosati, B.; Tarascon, J.-M. *Angew. Chem., Int. Ed.* **2008**, *47*, 2930.
(4) Winter, M.; Besenhard, J. O.; Spahr, M. E.; Novak, P. *Adv. Mater.* **1998**, *10*, 725.
(5) Huggins, R. A. *J. Power Sources* **1999**, *81*, 13.
(6) Limthongkul, P.; Wang, H.; Chiang, Y.-M. *Chem. Mater.* **2001**, *13*, 2397.
(7) Bryngelsson, H.; Eskhult, J.; Nyholm, L.; Herranen, M.; Alm, O.; Edström, K. *Chem. Mater.* **2007**, *19*, 1170.
(8) Park, C.-M.; Yoon, S.; Lee, S.-I.; Kim, J.-H.; Jung, J.-H.; Sohn, H.-J. *J. Electrochem. Soc.* **2007**, *154*, A917.
(9) Besenhard, J. O.; Hess, M.; Komenda, P. *Solid State Ionics* **1990**, *40*, 525.
(10) Tirado, J. L. *Mater. Sci. Eng., R.* **2003**, *R40*, 103.
(11) Fransson, L.; Vaughey, J. T.; Benedek, R.; Edström, K.; Thomas, J. O.; Thackeray, M. M. *Electrochem. Commun.* **2001**, *3*, 317.
(12) Alcántara, R.; Fernández-Madrigal, F. J.; Lavela, P.; Tirado, J. L.; Jumasb, J. C.; Olivier-Fourcade, J. *J. Mater. Chem.* **1999**, *9*, 2517.
(13) Fernández-Madrigal, F. J.; Lavela, P.; Pérez-Vicente, C.; Tirado, J. L. *J. Electroanal. Chem.* **2001**, *501*, 205.
(14) Fransson, L. M. L.; Vaughey, J. T.; Edstrom, K.; Thackeray, M. M. *J. Electrochem. Soc.* **2003**, *150*, A86.
(15) Yang, J.; Takeda, Y.; Imanish, N.; Yamamoto, O. *J. Electrochem. Soc.* **1999**, *146*, 4009.
(16) Li, H.; Shi, L.; Lu, W.; Huang, X.; Chen, L. *J. Electrochem. Soc.* **2001**, *148*, A91.
(17) Park, M.-S.; Needham, S. A.; Wang, G.-X.; Kang, Y.-M.; Park, J.-S.; Dou, S.-X.; Liu, H.- K. *Chem. Mater.* **2007**, *19*, 2406.
(18) Hewitt, K. C.; Beaulieu, L. Y.; Dahn, J. R. *J. Electrochem. Soc.* **2001**, *148*, A402.
(19) Zhao, X. B.; Cao, G. S. *Electrochim. Acta* **2001**, *46*, 891.
(20) Honda, H.; Sakaguchi, H.; Fukuda, Y.; Esaka, T. *Mater. Res. Bull.* **2003**, *38*, 647.

Published on Web 07/29/2009

active with different lithium reaction mechanisms, have been pursued. However, most of these intermetallic alloy anodes still exhibit capacity fade.

Here, we present a new class of Sb-MO_x-C (M = Al, Ti, or Mo) nanocomposite anodes that offer several advantages: (i) dispersion of ultrafine antimony metal particles in the MO_x-C ceramic matrix, which acts as a buffer to alleviate the volume expansion and (ii) low irreversible capacity loss in the first cycle as the formation of Li_2O is avoided. The Sb-MO_x-C nanocomposites are prepared by a simple high-energy mechanical milling (HEMM) of Sb_2O_3 with M (M = Al, Ti, or Mo) and C. The ultrafine antimony particles dispersed in the MO_x-C ceramic matrix are characterized by X-ray diffraction (XRD), transmission electron microscopy (TEM), X-ray photoelectron spectroscopy (XPS), and electrochemical charge−discharge measurements including impedance analysis.

Experimental Section

The Sb-MO_x-C (M = Al, Ti, or Mo) nanocomposites were obtained by a reduction of Sb_2O_3 (99.6%, Alfa) by aluminum (99.9%, 20 μm, Aldrich), titanium (99.9%, 150 μm, Aldrich), or molybdenum (99.9+%, 2 μm, Aldrich) metal powders in the presence of carbon (acetylene black) with a high-energy mechanical milling (SEPX vibratory mill) process at ambient temperature, as illustrated by reactions 1 −3 below:

$$Sb_2O_3 + 2Al \rightarrow 2Sb + Al_2O_3 \qquad (\Delta G^\circ = -944\ \text{kJ/mol}) \quad (1)$$

$$2Sb_2O_3 + 3Ti \rightarrow 4Sb + 3TiO_2 \qquad (\Delta G^\circ = -1384\ \text{kJ/mol}) \quad (2)$$

$$2Sb_2O_3 + 3Mo \rightarrow 4Sb + 3MoO_2 \qquad (\Delta G^\circ = -315\ \text{kJ/mol}) \quad (3)$$

The negative free-energy changes make the reduction reactions (1−3) spontaneous. Required quantities of Sb_2O_3 and M (in accordance with reactions 1−3) were mixed with acetylene black to offer a Sn-M:C weight ratio of 80:20 and then loaded with steel balls (diameter: $^1/_2$ and $^1/_4$ in.) into a hardened steel vial having a capacity of 80 cm^3 with a ball:powder ratio of 10:1 inside an argon-filled glovebox. The steel vial was then subjected to high-energy ball milling for 12 h at a speed of 1060 rpm. To look for iron contamination from the steel balls and vials, the samples were analyzed by energy-dispersive spectroscopy (EDS) attached to a scanning electron microscopy (SEM) system; the EDS data indicated a very low Fe concentration: < 0.5 wt %.

The phase analysis of the synthesized samples was performed using a Phillips XRD system with Cu Kα radiation. The morphology, microstructure, and composition of the synthesized powders were examined with a Hitachi S-5500 scanning transmission electron microscopy (STEM) system and a JEOL 2010F transmission electron microscopy (TEM) system. Surface characterization was performed with a Kratos X-ray photoelectron spectrometer (XPS) with a monochromatic Al Kα source.

The electrodes for the electrochemical evaluation were prepared by mixing 70 wt % active material (Sb-MO_x-C) powders, 15 wt % carbon black (Denka black) as a conducting agent, and 15 wt % poly(vinylidene fluoride) (PVDF) dissolved in *N*-methylpyrrolidinone (NMP) as a binder to form a slurry,

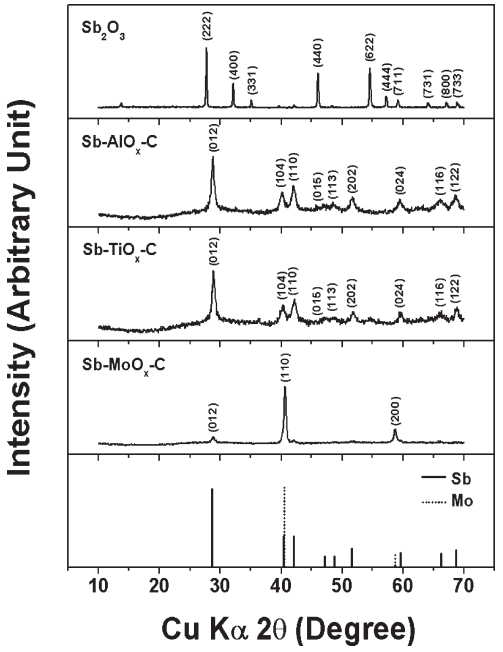

Figure 1. XRD patterns of pristine Sb_2O_3 and Sb-MO_x-C (M = Al, Ti, and Mo) nanocomposites obtained by the mechanochemical reduction reaction.

followed by coating on a copper foil, pressing, and drying at 120 °C for 3 h under vacuum. CR2032 coin cells were then assembled in an argon-filled glovebox with the cathodes thus prepared, Celgard polypropylene as a separator, lithium foil as the counter electrode, and 1 M $LiPF_6$ in ethylene carbonate (EC)/diethyl carbonate (DEC) (1:1 v/v) as the electrolyte. The discharge−charge experiments were performed galvanostatically at a constant current density of 100 mA/g of active material within the voltage range of 0−2 V vs Li/Li^+. To investigate any structural changes that may occur during electrochemical cycling, ex situ XRD data were collected after the electrodes were detached from the cell and it was covering with a polyimide tape as a protective film.

Electrochemical impedance spectroscopic analysis (EIS) was conducted using Solartron SI1260 equipment by applying a 10 mV amplitude signal in the frequency range of 10 kHz to 0.001 Hz. In the EIS measurements, the Sb-MO_x-C nanocomposite with an active material content of ~1.6 mg served as the working electrode and lithium foil served as the counter and reference electrodes. The impedance response was measured after different numbers of charge−discharge cycles (after 1 and 20 cycles), at 2 V vs Li/Li^+.

Results and Discussion

Characterization of the Nanocomposites. XRD patterns of the Sb-MO_x-C nanocomposites obtained via the mechanochemical reduction of Sb_2O_3 with Al, Ti, or Mo in the presence of acetylene black, according to reactions 1−3, are given in Figure 1. In the case of the nanocomposites with M = Al and Ti, all the diffraction peaks correspond to metallic antimony (JCDPS Powder Diffraction File Card No. No. 85-1323). In contrast, the XRD pattern shows reflections that correspond to both metallic antimony and molybdenum (JCDPS Powder Diffraction File Card No. No. 42-1120) in the case of the nanocomposite with M = Mo. In all three cases, no reflections that correspond to

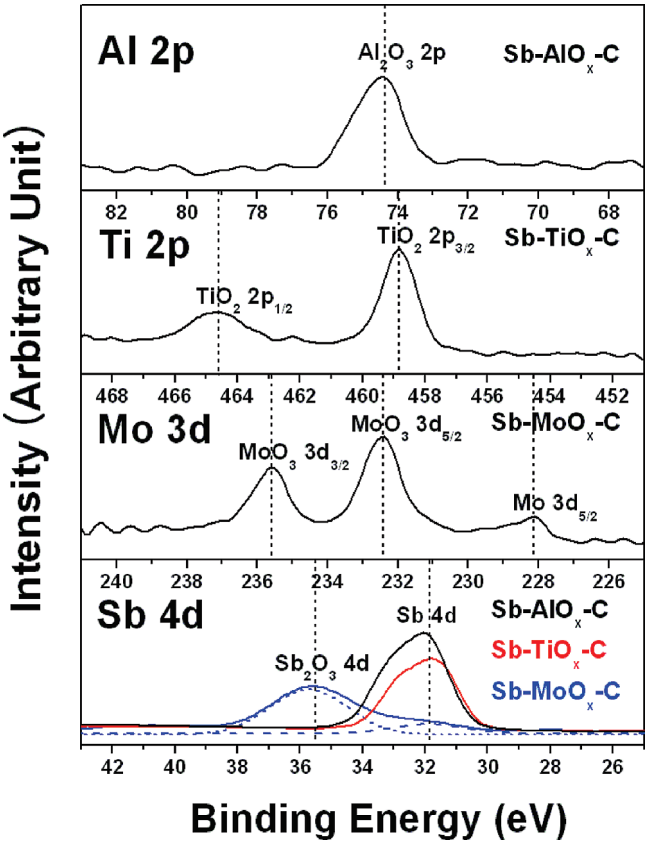

Figure 2. XPS spectra of the Sb-MO_x-C (M = Al, Ti, and Mo) nanocomposites.

oxides such as Al_2O_3, TiO_2, and MoO_2 (or MoO_3) could be observed, possibly because of their amorphous or poor crystallinity.

To have a better characterization of the amorphous phases present, all the nanocomposites were analyzed by XPS, as shown in Figure 2. While the Al 2p peak observed at 74.4 eV in the M = Al nanocomposite confirms the presence of Al_2O_3, the Ti $2p_{3/2}$ and $2p_{1/2}$ peaks that are observed, respectively, at 458.7 and 464.5 eV in the M = Ti nanocomposite confirm the presence of TiO_2. The M = Al and Ti nanocomposites also show the Sb 4d peak which corresponds to only metallic antimony at 31.9 eV, confirming the reduction of Sb_2O_3 completely to antimony. Thus, the combination of XRD and XPS data confirms the mechanochemical reduction of Sb_2O_3 by aluminum or titanium, in the presence of carbon, to give Sb + Al_2O_3 or Sb + TiO_2, in accordance with reactions 1 and 2. The amount of antimony in the nanocomposites, in accordance with reactions 1 and 2, is 57 and 54 wt %, respectively. However, in the case of M = Mo, the Mo $3d_{5/2}$ peak that corresponds to molybdenum at 228 eV, as well as the Mo $3d_{5/2}$ and $3d_{3/2}$ peaks that correspond to MoO_3 at 232.3 and 235.4 eV, respectively, are observed in Figure 2. The formation of MoO_3, instead of the anticipated MoO_2 (in accordance with reaction 3), is due to the higher negative standard free energy for the formation for MoO_3 (−767 kJ/mol), compared to that for MoO_2 (−603 kJ/mol). The M = Mo sample also shows broad Sb 4d peaks in Figure 2 that correspond to both Sb_2O_3 and antimony at,

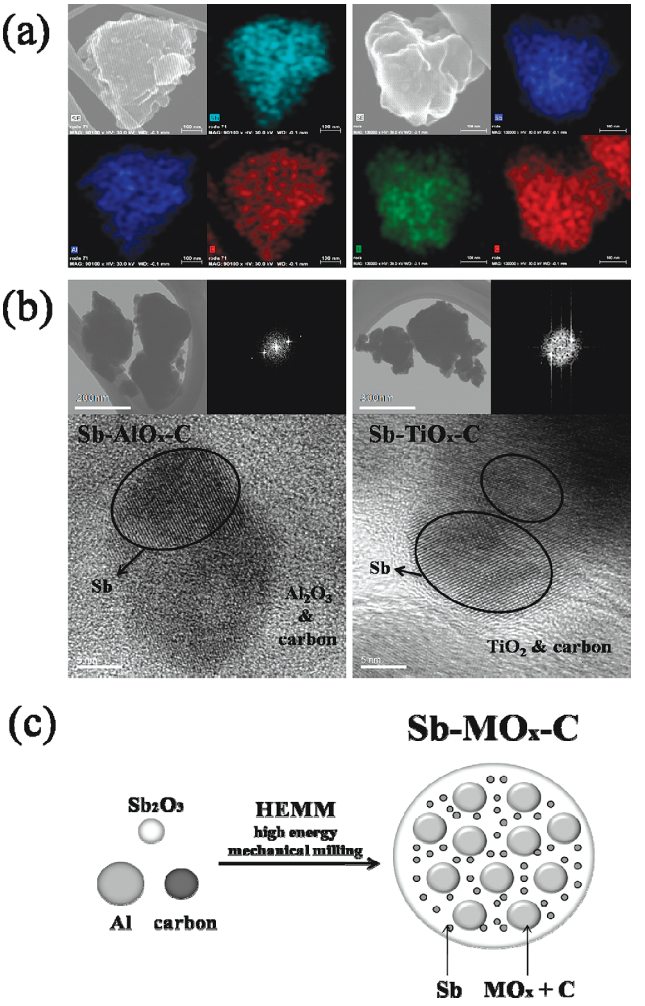

Figure 3. (a) STEM images, (b) HRTEM images, and (c) schematic description of the Sb-MO_x-C (M = Al and Ti) nanocomposites. Also shown are the fast Fourier transform (FFT) images over selected regions.

respectively, 35.7 and 31.9 eV. Because the amounts of Sb_2O_3 and molybdenum in the reaction mixture were chosen according to reaction 3, part of the molybdenum metal in the reaction mixture remains underutilized. Also, the presence of Sb_2O_3, as indicated by the XPS data, reveals that the reduction reaction of Sb_2O_3 by Mo may be incomplete under the mechanochemical reduction conditions. This conclusion is consistent with the XRD peak seen in Figure 1 for metallic molybdenum in the M = Mo sample. Thus, the Sb-MO_x-C nanocomposite with M = Mo consists of antimony, Sb_2O_3, molybdenum, MoO_3, and carbon, unlike the nanocomposites with M = Al and Ti.

Figure 3a shows the STEM images of the M = Al and Ti samples. Although agglomeration has occurred, the presence of single particles ~500 nm in size could be visualized. The reduced antimony, MO_x, and carbon are homogeneously dispersed in the nanocomposites. Figure 3b shows the high-resolution images of the nanocomposites, along with fast Fourier transform (FFT) images that correspond to the selected regions. The crystalline antimony phase is confirmed by the FFT image, which agrees with the XRD data in Figure 1. Also, the reduced crystalline antimony phase with particles 15−20 nm in size is

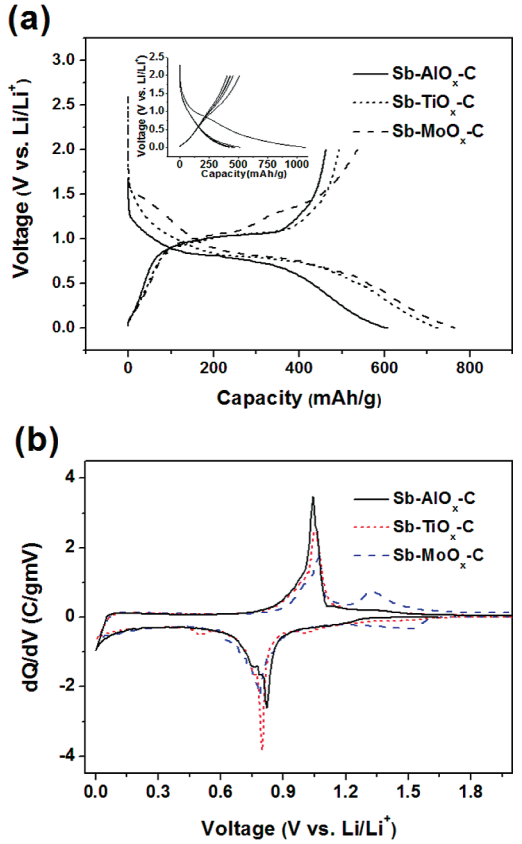

Figure 4. Comparison of the (a) discharge−charge profiles and (b) differential capacity plots (DCP) of the Sb-MO_x-C (M = Al, Ti, and Mo) nanocomposites.

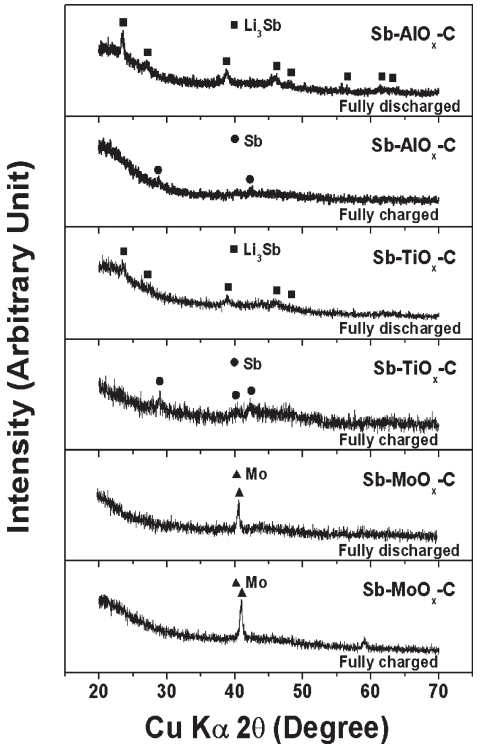

Figure 5. XRD data of the Sb-MO_x-C (M = Al, Ti, and Mo) nanocomposites after first discharge (Li insertion) and after first charge (Li extraction).

well-surrounded by the amorphous MO_x oxide and carbon phases. This homogeneously mixed morphology, as shown by the schematic description in Figure 3c, may be beneficial to provide good electrical contact with the current collector, as well as a buffering effect on the volume expansion−contraction that occurs during cycling.

Electrochemical Properties. Figure 4a compares the first discharge−charge profiles of all the three Sb-MO_x-C nanocomposites. The voltage profiles of the M = Al and Ti samples are similar to that observed for a pure antimony electrode, with an average discharge−charge voltage of ~0.9 V. The M = Al and Ti nanocomposites show first discharge capacities of, respectively, 607 and 724 mAh/g and first charge capacities of, respectively, 463 and 491 mAh/g, which implies initial Coulombic efficiencies of, respectively, 76% and 68%. The M = Mo nanocomposite exhibits the discharge−charge profiles of both antimony and Sb_2O_3, together with first discharge and charge capacities of, respectively, 765 and 537 mAh/g, implying an initial Coulombic efficiency of 70%. To determine the contribution of acetylene black in the nanocomposites, we also investigated the electrochemical behavior of acetylene black after milling for 12 h under identical conditions. The inset in Figure 4a shows the discharge−charge profiles of the ball-milled acetylene black. It exhibits a first discharge capacity of ~200 mAh/g, which decreases to approximately one-third of that value in the next cycles, as seen in the inset of Figure 4a. Based on reactions 1 and 2, the expected amounts of Al_2O_3 and TiO_2 in the M = Al and Ti nanocomposites is, respectively, 23 and 26 wt %. While Al_2O_3 is known to be electrochemically inactive, TiO_2 (26 wt % in the Sb-TiO_2−C composite) is expected to contribute ~55 mAh/g, which corresponds to the formation of Li_xTiO_2 with $x \approx 0.5$. However, the contributions of Sb_2O_3 and MoO_3 in the M = Mo nanocomposite could not be assessed, because we could not estimate the relative amounts of Sb_2O_3 and MoO_3 in the nanocomposite.

With an objective to fully understand the discharge−charge process, the differential capacity plots (Figure 4b) of the first cycle were analyzed for all three nanocomposites. The differential discharge plots show a broad peak from 1.3 V to 0.8 V, which is related to the formation of a solid−electrolyte interfacial (SEI) layer, which is due to electrolyte decomposition on the surface of the active material. The major reduction (alloying) and oxidation (dealloying) peaks at, respectively, ~0.8 V and ~1 V correspond to the reaction of lithium with metallic antimony in the Sb-MO_x-C nanocomposite. These peaks are shifted slightly, compared to that observed with pure antimony metal, possibly due to the reduction in electrical conductivity by the ceramic oxide matrix. The electrochemical process of the amorphous carbon with lithium appears as a broad peak below 0.2 V.[17] With the M = Mo nanocomposite, an additional broad reduction and oxidation peak occurs at ~1.5 V and ~1.3 V, respectively, because of the reaction of Sb_2O_3 with lithium.

Figure 5 presents an ex situ XRD analysis that has been performed on fully lithiated and delithiated electrodes for

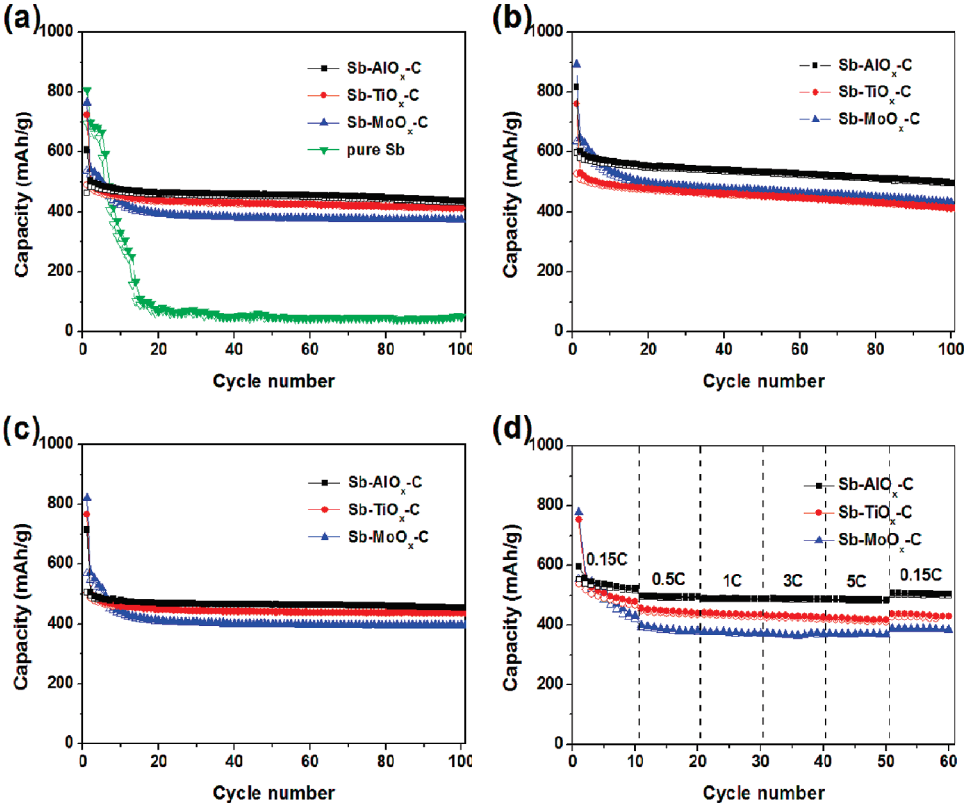

Figure 6. Comparison of the cycling performances of the Sb-MO_x-C (M = Al, Ti, and Mo) nanocomposites (a) at 25 °C at C/5 rate, (b) at 55 °C at C/5 rate, (c) at 25 °C at C/5 rate in the presence of 300 ppm Mn^{2+} in the electrolyte, and (d) at 25 °C under various C rates.

Table 1. Electrochemical Performances of the Sb-MO_x-C (M = Al, Ti, and Mo) Nanocomposites

	Sb-AlO_x-C	Sb-TiO_x-C	Sb-MoO_x-C
At 25 °C			
discharge capacity (mAh/g)	607	724	765
charge capacity (mAh/g)	463	491	537
first cycle efficiency (%)	76	68	70
capacity retention after 100 cycles (%)	93	83	70
At 55 °C			
discharge capacity (mAh/g)	815	761	896
charge capacity (mAh/g)	596	503	635
first cycle efficiency (%)	73	66	71
capacity retention after 100 cycles (%)	83	78	68
At 25 °C in the Presence of 300 ppm Mn^{2-}			
discharge capacity (mAh/g)	715	765	820
charge capacity (mAh/g)	506	503	570
first cycle efficiency (%)	71	66	70
capacity retention after 100 cycles (%)	90	87	69

all the Sb-MO_x-C nanocomposites. The XRD data of the M = Al and Ti nanocomposites show the formation of only the Li_3Sb phase at the end of discharge (i.e., when the potential reached 0 V). After the charge, the Li_3Sb phase disappears and only the Sb phase is observed. However, it is rather difficult to identify the Li_3Sb phase in the XRD data of the M = Mo nanocomposite during the first few cycles.

Figure 6 compares the cyclability of the three Sb-MO_x-C nanocomposites between 0 V and 2 V at a constant current of 100 mA/g (C/5 rate), while Table 1 presents the gravimetric capacity, Coulombic efficiency in the first cycle, and capacity retention after the 100th cycle, under various conditions. While pure antimony exhibits continuous capacity fade within 20 cycles, all three Sb-MO_x-C nanocomposites show good cyclability at 25 and 55 °C (see Figures 6a and 6b). Although the capacity values increase significantly when going from 25 °C (Figure 6a) to 55 °C (Figure 6b), because of the enhanced electrochemical activity and kinetics of the Sb-MO_x-C nanocomposites at higher temperatures, the capacity retention decreases slightly, possibly because of the enhanced reaction with the electrolyte. Particularly, the M = Al composite exhibits better capacity retention, compared to the M = Ti and Mo nanocomposites. It retains 93% capacity after 100 cycles at 25 °C. The better performance of the M = Al nanocomposite, despite the significantly lower electronic conductivity of Al_2O_3, compared to TiO_2 or MoO_3, may be related to the better mechanical properties of Al_2O_3, such as tensile strength and fracture toughness; however, Al_2O_3 remains as an insulator during the entire charge discharge process, and the formation of Li_xTiO_2 and Li_xMoO_3 during the discharge process can enhance the electronic conductivity. For instance, some reinforced ceramic−metal composites are known to exhibit high strength, high modulus, and enhanced resistance to fatigue crack growth.[21,22] In this system, the enclosure or

(21) Chen, D. L; Chaturvedi, M. C.; Goel, N.; Richards, N. L. *Int. Fatigue* **1999**, *21*, 1079.
(22) El-Eskandarany, M. S. *J. Alloys Compd.* **1998**, *279*, 263.

dispersion of the fine particles of the electrochemically active antimony metal within or among the ceramic oxide and carbon matrix leads to enhanced capacity retention.[23] The ceramic oxide and carbon provide a stable, structurally inactive matrix that buffers against the volume expansion−contraction and impedes the growth of the electrochemically active antimony nanoparticles during cycling, while the conductive carbon offers the necessary electronic conduction pathway. In addition, the stable SEI film formed on carbon could also help to maintain good electrochemical performance during cycling.

One of the difficulties with the $LiMn_2O_4$ spinel cathodes is the poisoning of the carbon anode by the dissolved Mn^{2+} ions from the cathode lattice during cycling. Accordingly, we also assessed the cyclability of all three Sb-MO_x-C nanocomposite anodes at 25 °C in the presence of 300 ppm Mn^{2+} in the electrolyte, i.e., the experiments were performed by purposely adding the required amount of anhydrous manganese perchlorate salt to the electrolyte (to give 300 ppm Mn^{2+}) before assembling the cell. As seen in Figure 6c, the cyclabilities of the nanocomposite anodes do not differ significantly on adding Mn^{2+}, which suggests that these nanocomposite anodes may not be poisoned by Mn^{2+} and they may have the potential to be used with manganese spinel cathodes in lithium-ion cells.

Figure 6d compares the rate capabilities of all three Sb-MO_x-C nanocomposites at various C rates (from 0.15C to 5C rates; 0.5C rate means utilizing the capacity in 1/0.5 (or 2) h, while 5C rate means utilizing the capacity in 1/5 (or 0.2) h). All three nanocomposites exhibit excellent rate capability at 25 °C. Especially, the M = Al nanocomposite retains a high capacity of ~489 and ~487 mAh/g at 3C and 5C rates, respectively, with stable cycling.

To gain further insight into electrochemical performances, EIS measurements were conducted at 2 V vs Li/Li^+ with all three Sb-MO_x-C nanocomposite samples before cycling and at different cycles (after the 1st cycle and the 20th cycle). The EIS data were analyzed based on an equivalent circuit given in Figure 7a,[24] where R_u refers to uncompensated resistance between the working electrode and the lithium reference electrode, CPE_s refers to the constant phase element of the surface layer, R_s refers to the resistance of the SEI layer, CPE_{dl} refers to the CPE of the double layer, R_{ct} refers to the charge-transfer resistance, and Z_w refers to the Warburg impedance. Generally, the EIS spectrum can be divided into three frequency regions, i.e., low-frequency, medium-to-low-frequency, and high-frequency regions, which correspond, respectively, to cell geometric capacitance, charge transfer reaction, and lithium-ion diffusion through the surface layer. The EIS spectra recorded before cycling, after the 1st cycle, and the 20th cycle in Figure 7b consist of one semicircle and a line. The diameter of the semicircle is a measure of the charge-transfer resistance R_{ct}, which is

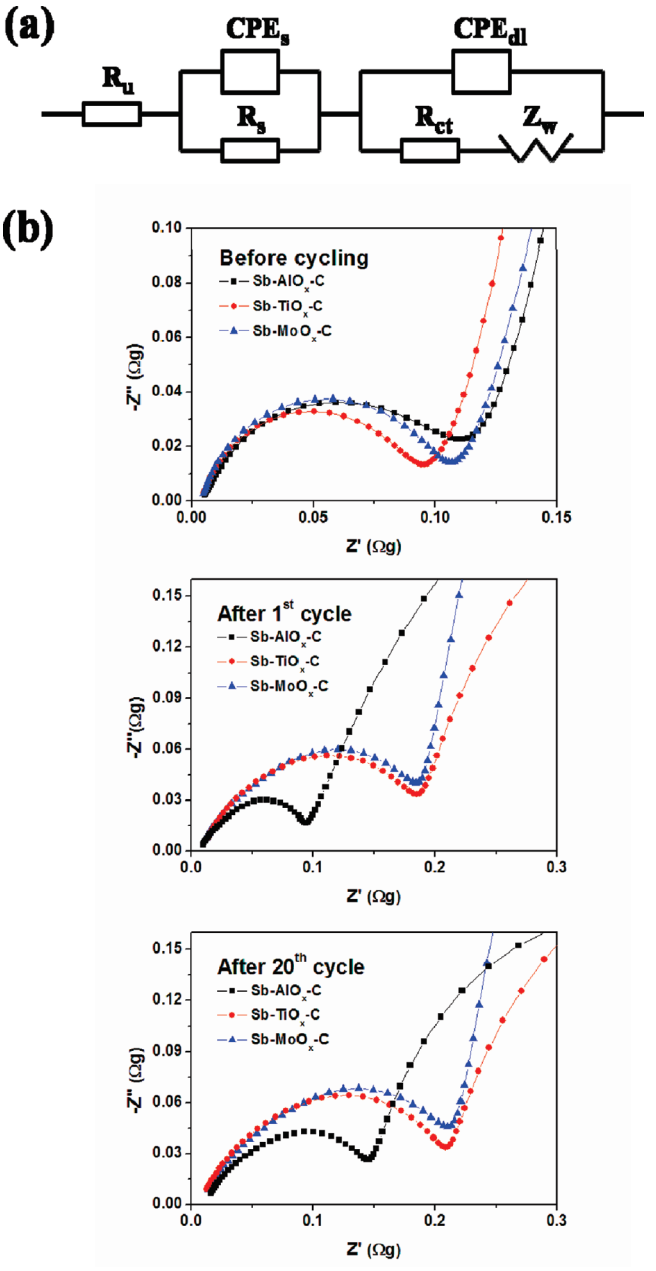

Figure 7. (a) Equivalent circuit for the Sb-MO_x-C (M = Al, Ti, and Mo) nanocomposites and (b) electrochemical impedance spectra (EIS) of the nanocomposites before cycling, after the 1st cycle, and after the 20th cycle.

related to the electrochemical reaction between the particles or between the electrode and the electrolyte. On the other hand, the sloping line is related to lithium-ion diffusion in the bulk of the active material. The diameter of the semicircle increases when going from the pristine electrode (before cycling) to that subjected to 20 cycles, which indicates an increase in R_{ct} as the electrode is cycled, possibly because of the breaking of the interparticle contact caused by the volume expansion. Among the three nanocomposites investigated, although the M = Al nanocomposite exhibits the highest charge-transfer resistance before cycling, because of the electrochemical inactivity and insulating behavior of Al_2O_3, compared to those of TiO_2 and MoO_3, it shows the lowest charge-transfer resistance after the 1st and 20th cycles (0.1 and

(23) Jung, G.-J.; Kim, Y. U; Sohn, H.-J.; Kang, T. *J. Power Sources* **2001**, *101*, 201.
(24) Liu, J.; Manthiram, A. *Chem. Mater.* **2009**, *21*, 1695.

0.17 Ω g, respectively, after the 1st and 20th cycles). This implies that Al_2O_3 is more effective in accommodating the volume expansion smoothly and impeding the particle growth of antimony, compared to TiO_2 and MoO_3, which is consistent with the cyclability data shown in Figure 6.

Conclusions

Sb-MO_x-C (M = Al, Ti, and Mo) nanocomposites synthesized by a mechanochemical reduction of Sb_2O_3 with aluminum, titanium, or molybdenum, in the presence of acetylene black carbon, have been investigated as an anode material for lithium-ion batteries. Characterization data collected with XRD, XPS, TEM, and STEM reveal a uniform dispersion of the antimony nanoparticles within the MO_x and conductive carbon matrix. The Sb-MO_x-C nanocomposite exhibit excellent electrochemical performances, with the M = Al nanocomposite offering a capacity of >430 mAh/g after 100 cycles. The buffering effect provided by the amorphous metal oxide and conductive carbon matrix mitigates the problems normally encountered with the volume changes that occur during cycling and leads to good electrochemical performance. The study demonstrates that the problems normally encountered with the huge volume expansion associated with the alloy anodes could be minimized by a rational design of nanocomposite microstructures.

Acknowledgment. This work was supported by the Office of Vehicle Technologies of the U.S. Department of Energy (under Contract No. DE-AC02-05CH11231).